Experiments in Fluids (2026) 67:185
https://doi.org/10.1007/s00348-026-04348-2

RESEARCH ARTICLE

Pendant drop rotation in vertical, turbulent, shearing flows

Jacob D. Dockery[1] · Sagar Gharti[2] · Michael P. Kinzel[2] · Andrew K. Dickerson[1]

Received: 10 June 2026 / Revised: 4 September 2026 / Accepted: 19 October 2026
© The Author(s), under exclusive licence to Springer-Verlag GmbH Germany, part of Springer Nature 2026

Abstract

In natural and engineering applications, mobile drops frequently encounter nonuniform flows, and such interactions are both uncharacterized and difficult to experimentally observe. In this study, we record the dynamics of pendant drops (drop of liquid suspended from the end of a needle), a natural and ubiquitous drop state, subject to the non-uniform disturbances of aerodynamic turbulence and shear. Our turbulent, shearing flow is formed by a pseudo-coaxial jet. By protruding a co-flowing jet through the center of a suction-type vertical wind tunnel, we create a novel flow field termed sheathed, coaxial jet-flow (SCJF). Tuning the jet (core) and tunnel (sheath) velocities allows us to create turbulent, shearing flow fields that arise from the interactions at the flow interface. We employ an Eulerian-based finite-volume CFD solver within to characterize our novel flow and understand the drop dynamics therein. Subject to turbulent, shearing flows, pendant drops may rotate. The onset of drop rotation is influenced by turbulence below a threshold Reynolds number defined by the needle diameter. We find that pendant drop dynamics in SCJF are influenced by the size of the capillary support, the velocity ratio between the core and sheath, the drop size, and the magnitudes of turbulence intensity and shear imposed on the drop. We find that pendant drops exhibit limited modal behavior compared to that observed for laminar conditions and that small drops rotate faster than large drops. We form a scaling argument based upon the energetics of a rotating drop to reveal that dimensionless drop rotation, given by a modified Strouhal number, scales with an inverse drop Reynolds number. By comparing our results to the findings of our previous work in laminar flows, we discover that turbulence does not notably influence dimensionless drop rotation.

1 Introduction

Drops suspended from needles, pendant drops, have received much attention in recent decades due to their suite of applications. Understanding the dynamics of pendant drops is crucial for environmental studies (Omid Mosalman Haghighi et al. 2020; Latif and Brimblecombe 2004), lab-on-a-chip devices (Yang et al. n.d.), ink-jet printing (Wijshoff 2018), pharmaceutics (Madhuvanthi et al. 2010; Schmit et al. 2014), and surface tension measurements (Pan et al. 2025). Additionally, pendant drops provide a convenient platform by which to characterize the interaction of drops with aerosols (Speirs et al. 2023), gaseous species (Killion and Garimella 2005), and flow structures (Dockery et al. 2024). Continuous attachment to the capillary allows pendant drops to be enlarged (Lee and Hwang 2025), retracted (Willmott et al. 2011), released (Xie et al. 2025; Henderson et al. 1997), charged (Ferrera et al. 2013), and held in steady view (Lee and Hwang 2025) while subject to a wide range of conditions. Phenomena surrounding pendant drops, such as their natural frequency (Parkinson and Phan 2018), shape perturbations (Osman et al. 1994), rotational dynamics (Dockery et al. 2024; Lee and Hwang 2025), jetting transition (Clanet and Lasheras 1999), stability (Zhang and Zhou 2023), and pinch-off (Taraki and Ismail 2026), have been characterized for ambient and uniform conditions, but the dynamics of pendant drops in response to more dynamic external perturbations is considerably less explored. Investigations concerning pendant drop dynamics in response to external disturbances have been limited to uniform disturbances such as laminar flows (Lee and Hwang 2025; Dockery et al. 2024), acoustic waves (Bussonnière et al. 2016), and movement of the capillary support (Edward et al. 2001), with no attention diverted to pendant drop dynamics in response to more dynamic, inharmonic disturbances. In this study, we subject pendant drops to the non-uniform disturbances of turbulent, shearing flow and record their dynamics as shown in Fig 1a.

✉ Andrew K. Dickerson
ad@utk.edu

[1] Mechanical and Aerospace Engineering, University of Tennessee, Knoxville, USA

[2] Aerospace Engineering, Embry-Riddle Aeronautical University, Daytona Beach, USA

Published online: 02 November 2026

Exposed to external forces, pendant drops deform, rotate, and shear. In acoustic fields, pendant drops exhibit longitudinal, translational, and rotational modes (Moon et al. 2006). The resonance frequency at which pendant drops experience longitudinal and rotational modes is a function of drop size, in which increasing drop size decreases the resonant frequency (Moon et al. 2006). In ascending laminar flows parallel with gravity and the supporting needle, pendant drops rotate and experience deformation quantified by a variety of behavioral modes (Dockery et al. 2024; Lee and Hwang 2025). In our previous study with ascending laminar flows, pendant drop rotation was shown to be influenced by wind speed, needle diameter, drop diameter, wettability of the straight-cut needle, and liquid surface tension (Dockery et al. 2024). Shape deformation was shown to coincide with small rotational amplitudes compared to the needle (Dockery et al. 2024). Through experiment and modeling, Lee and Hwang showed that pendant drop dynamics and equilibrium shapes at a fixed velocity are influenced by the longitudinal length of the pendant drop, the distance from the tip of the needle to the drop apex (Lee and Hwang 2025). They highlight the existence of critical longitudinal drop lengths that denote regions of stability and instability for a fixed wind speed based upon the variation of the tilting angle of the drop. Lacking in the study of pendant drop response to external perturbation is the drop response to more dynamic, less uniform excitation.

Raindrops, a close relative to hanging (or pendant) drops, have been characterized in response to both uniform and non-uniform disturbances. Falling through the atmosphere, raindrops are subject to both laminar (uniform) and turbulent (nonuniform) flows, in which they experience shape deformation (Szakall et al. 2009), breakup (Emersic and Connolly 2011), coalescence (Testik et al. 2011), and oscillations (Szakall et al. 2010). Turbulence augments drop canting angle, axis ratio, fall speed, and drop oscillation compared to that which would occur in laminar conditions (Zheng et al. n.d.). Similarly stated, non-uniform disturbances augment the drop response from those observed from uniform disturbances of the same medium. Subsequently, we expect the pierced counterparts of levitating drops to show augmented behavior from that observed in laminar flow.

In this study, we subject pendant drops to a shearing, turbulent flow. The sheared, turbulent flow is created by the interaction between a core jet and a co-flowing sheathing airstream: a novel flow field that we have coined the sheathed coaxial jet-flow (SCJF). Our SCJF is similar to a coaxial jet. Coaxial jets are characterized by a core jet that is encircled by a sheath jet (René Van Hout et al. 2021). Coaxial jet characteristics are well described by the interaction between two potential core flows, schematized in Fig.1b. The velocity ratio between the core and jet r_U, the diameter ratio r_D, and the outright core U_C and sheath U_S velocities influence conditions downstream of the outlet (René Van Hout et al. 2021). Shear between the core, sheath, and ambient surroundings leads to turbulence, vorticity, and breakdown of the potential cores (Villermaux and Rehab 2000). Even when $r_U = 1$, the lip-thickness between the two flows gives rise to wake-like instabilities downstream (Angelin et al. 2025). The influence of the sheath flow upon the inner potential core length is given by e, which stands as the ratio between the potential core length with and without a sheath flow present (Au and Ko 1987). Generally, when $r_U < 1$, the inner potential core is lengthened by the presence of the sheath flow. When $r_U > 1$, e falls below unity once r_U is sufficiently large and e is greatly influenced by r_D (René Van Hout et al. 2021). Downstream of the inner core breakdown, the two flows continue to mix and merge until the flow becomes fully developed. Once the flows have merged, there is a distance from the jet outlet at which the flow profile matches that of a singular jet (Kwan and Ko 1976).

We create our sheathed, coaxial jet flow by allowing the core flow to exhaust into the sheath flow, rather than having both the core and sheath jet into ambient conditions. By augmenting the physical dimensions of a coaxial jet, we create our shearing, turbulent flow. We radially expand the sheath diameter of the coaxial jet in Fig. 1b and offset the plane of the core jet exit from that of the sheath to create our sheathed, coaxial jet flow, schematized in Fig. 1c. In our case, the sheath flow boundary is the wall of the vertical wind tunnel, and the core jet is provided by a thin-walled tube protruding through the tunnel. We employ a computational model to characterize our novel flow and to provide numerical values for downstream conditions such as turbulent intensity and a velocity field. Additionally, we physically suspend drops at different heights above the core jet exit and record pendant drop motion in response to the aerodynamic, non-uniform disturbance.

2 Methods

2.1 Experimental setup

In this study, we investigate the oscillatory behavior of pendant drops exposed to sheath flow. The pull-type vertical wind tunnel from Dockery et al. 2024 was augmented to allow for the interaction of a core and sheath flow and equipped with a secondary 8" duct fan. The augmented vertical wind tunnel is shown in Fig. 2. The sheath flow, induced by a dual fan system, is controlled with an ITech IT-M7721L variable AC power supply and a 2000-VA (Volt-Amperes) secondary voltage regulator. The sheath flow is pulled through a HEPA filter, laminarizer, and contraction section prior to entering the observation section measuring 12 x 12 cm. The half-width f of the two-dimensional contraction in centimeters is defined by $f(z) = -1.2\times10^{-7}z^6+8.9\times10^{-6}z^5-1.7\times10^{-4}z^4+15$,

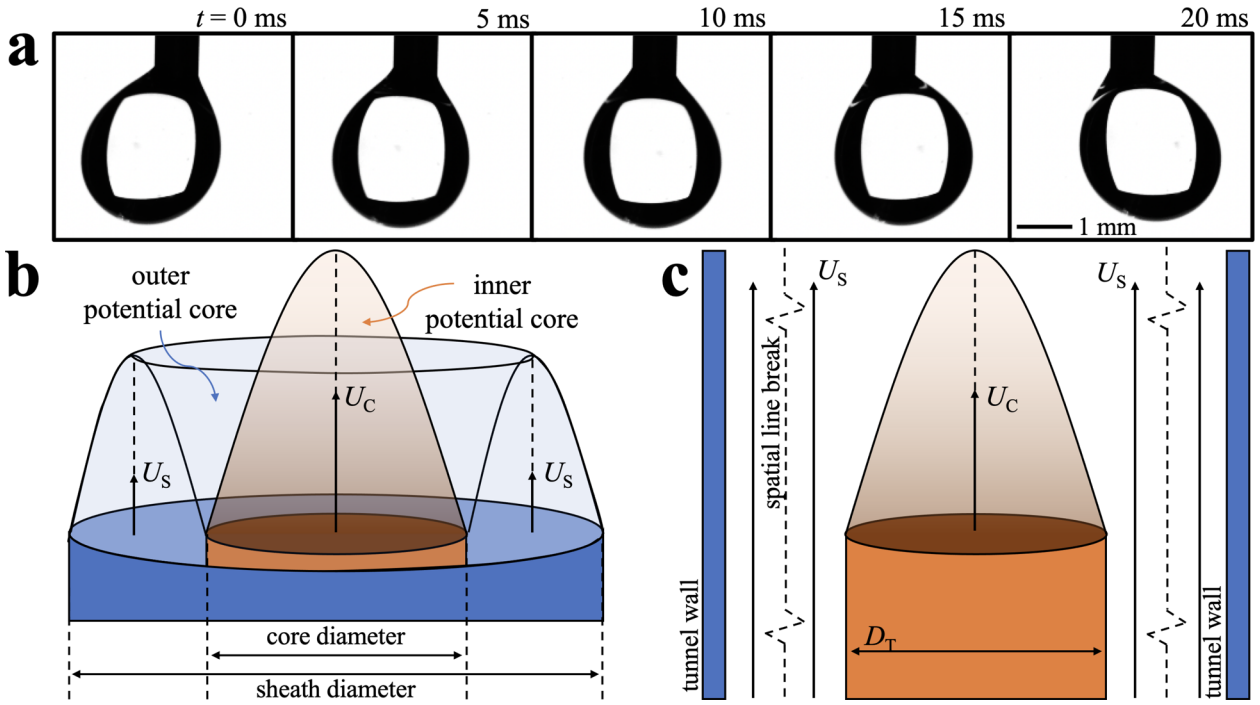

Fig. 1 Pendant drops may oscillate when exposed to turbulent, shearing flow. **a** Time schematic of a drop of diameter 2.5 mm rotating 15.9 cm above the coaxial jet with a velocity of 4 m/s and a sheath flow velocity of 0.8 m/s. Our shearing, turbulent flow is created by a sheathed, coaxial jet-flow, which is similar to a coaxial jet shown in **b**. By allowing a core jet to protrude and exhaust into a vertical wind tunnel, we create a sheathed, coaxial jet-flow shown in **c**

where z [cm] is the axial dimension of the contraction and $z = 0$ corresponds to the contraction inlet (Je Sargison et al. 2004). More details concerning the tunnel dimensions can be found in our previous article (Dockery et al. 2024). Sheath flow velocity U_S is measured using a TSI Velocicalc anemometer with 0.01-m/s precision. The core flow is supplied by a $D_T = 1.27$-cm diameter brass tube with a 0.56-cm wall thickness. The presence of the tube in the observation section reduces the sheath flow cross section by $\approx 1\%$. Honeycomb laminarizers with a cell width of $D_C = D_T/4$ are staggered in three layers, forming a combined thickness of 3.6 cm, and are placed at the exhaust of the tube. The range of tube Reynolds numbers varies from $Re_T = 340 - 4700$, indicating that our tube flow ranges from laminar to turbulent without the laminarizer in place. For our highest Re_T, the Reynolds number within the honeycomb is $Re_C = 1175$, which reduces the turbulent pipe flow to a laminar but not fully developed exhaust. Since the honeycomb is flush with the tube outlet, the micro-jets created by the honeycomb are not given the opportunity to dissipate within the tube. The tube penetrates the HEPA filter, honeycomb laminarizers, and contraction section such that its position is viewable and controllable within the observation section. The core flow is supplied by the flow diagram depicted in Fig. 2b. The core flow velocity U_C is measured using a TSI model 4043 flow meter. Centered above the tube exit, a drop of diameter D is extruded onto a needle of diameter D_N using a New Era NE-800 syringe pump as shown in Fig. 2c. Pendant drop motion is backlit and then captured at 1000 fps using a Photron Nova S6 high-speed camera attached with a 105 mm 1:2.8 Sigma lens. We record drop rotation at 3 heights above the tube outlet $L = 32$, 16, and 2 cm that correspond to named locations, L1, L2, and L3, and are equivalent to $L/D_T = 25.2$, 12.6, and 1.57, respectively. Drops at each location are subject to velocity fields characterized by $r_U = 0.2, 0.4, \ldots, 1.4$ and $U_S = 2, 4$ m/s, except at L3 where $r_U = 0.2, 0.4$ are untested for $D_N = 0.08$ cm.

Videos of drop motion are binarized and analyzed using bespoke code in MATLAB. Using the needle as a physical scale, we track the drop centroid x_0, drop volume V_D, and angular velocity ω. The drop angular velocity is calculated by tracking the lateral position of x_0 and is averaged across a minimum of 1.5 periods. Lateral position from one camera is sufficient to measure angular velocity because drops do not simply oscillate laterally, but draw circles as they swing below the needle (Dockery et al. 2024). We display the rotational motion of a pendant drop in Fig. 3a and plot the lateral position of the centroid x_o against time in Fig. 3b. We calculate the frequency of oscillation $f = (2T_{1/2})^{-1}$, where $T_{1/2}$ is the half the period of rotation, the time between each oscil-

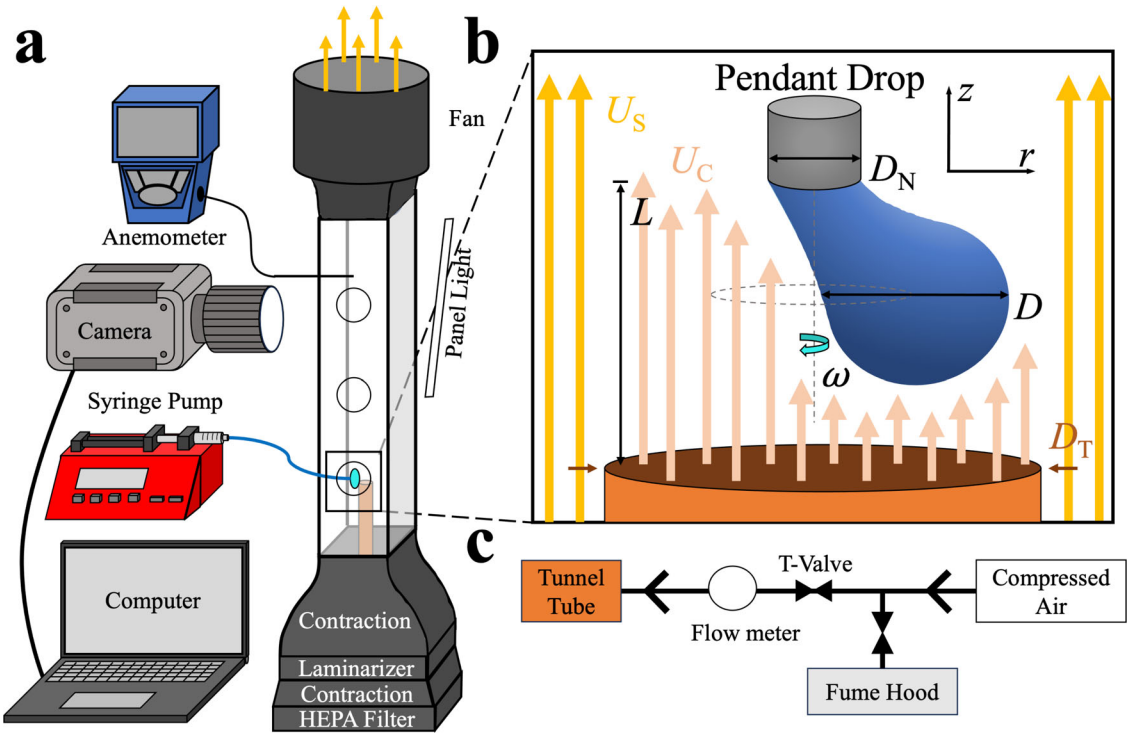

Fig. 2 Schematic of experimental setup displaying pertinent dimensions and flow system. **a** Vertical wind tunnel wherein drop oscillation in sheath flow is investigated. **b** Zoom square depicting pertinent dimensions of a pendant drop, core and sheath flow. **c** Pictorial diagram of the system used to deliver laminarizer core flow

latory apex. The drop in Fig. 3 has a mean $T_{1/2} = 43.5 \pm 0.5$ ms. Such consistency in drop rotation allows us to minimize the length of each video and calculate $\omega = 2\pi f$ from a minimum of 1.5 periods.

Drop volume V_D is calculated using the second theorem of Pappus (Dockery et al. 2024) at the instant when the two-dimensional cross section of the drop is intersected by a plane parallel to the lens. Such a method relies on an accurate binarization of the drop shadow. We estimate that the uncertainty in the drop boundary following binarization is one pixel of length $\Delta r = 0.02 \pm 0.001$ mm along the contour of the drop shadow. In the instance that every pixel along the drop shadow is uncertain, the uncertainty in drop volume is a shell one pixel thick, we approximate as a sphere (Rible et al. 2026), with volume $V_{unc} \approx \pi D^2 \Delta r$. The percent error is $V_{unc}/V_D \approx \Delta r/D$. In the case of our smallest drop, $D \approx 1$ mm, $V_{unc}/V_D \approx 2\%$. The percent error decreases as D increases.

2.2 Computational approach for characterizing tunnel conditions

We employ the commercial CFD code Star-CCM+ to characterize the flow delivered to the pendant drop at test locations in the tunnel. An Eulerian-based finite-volume CFD solver is used to provide pressure and velocity fields. Conservation of mass and the Navier–Stokes equations are solved simultaneously in axisymmetric cylindrical coordinates using a finite-volume discretization, where the geometric source terms arising from axisymmetry are automatically accounted for by the Star-CCM+ solver. The simulations are executed using a steady-state, segregated, pressure-based solver. The SIMPLE algorithm (Patankar and Spalding 1972) is employed for pressure–velocity coupling, and second-order spatial discretization schemes are used for the momentum equation to ensure adequate accuracy. Convergence is assessed by monitoring the residual levels for continuity, momentum, turbulent kinetic energy, and specific dissipation rate, with a convergence criterion of 10^{-5} for all scaled residuals. Air is modeled as an incompressible, Newtonian fluid with a density of $\rho_a = 1.27$ kg/m^3 and a dynamic viscosity of $\mu_a = 1.8 \times 10^{-5}$ Pa · s. Turbulence is represented using the k–ω SST model developed by Menter (Menter 1994), which blends the k–ω formulation near the solid walls with the k–ε model in the freestream. This blended formulation makes the SST model well-suited to this problem, providing accurate resolution of the shear layer at the core-sheath interface while maintaining robustness under the adverse pressure gradients present near the jet exit region.

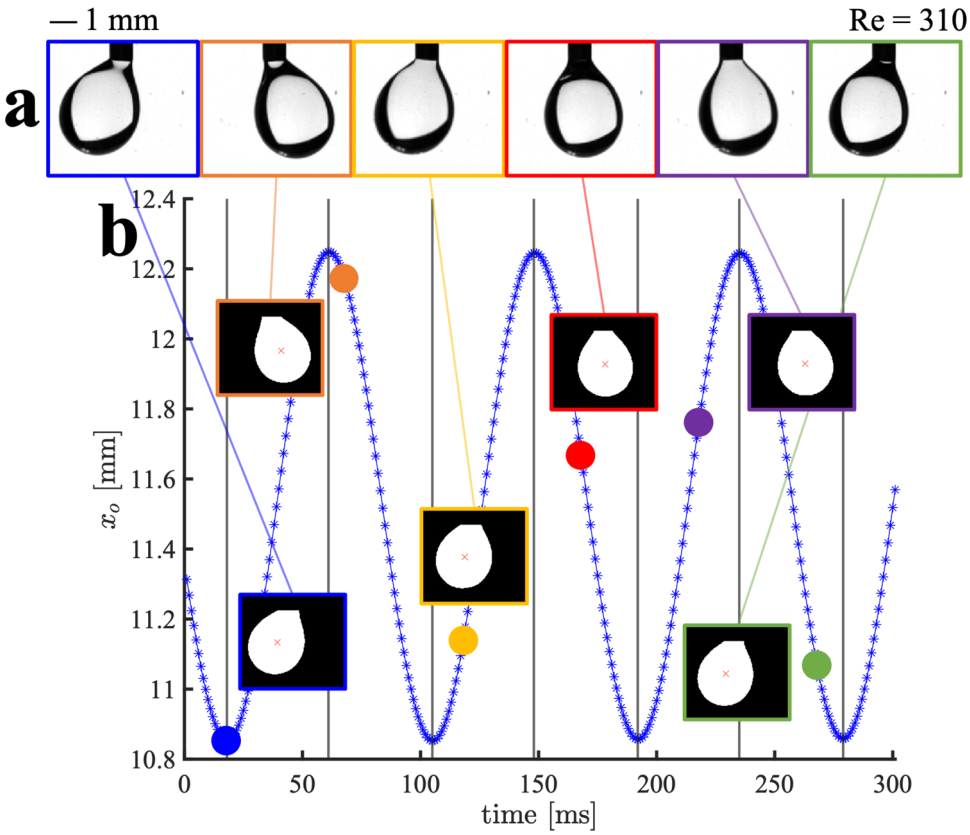

Fig. 3 Drop rotation is quantified by tracking the drop centroid throughout rotation. **a** Image sequence of drop of Re = 310 rotating at $\omega = 72$ rad/s on a needle of diameter $D_N = 0.08$ cm. **b** The lateral position of the centroid x_o is plotted against time. Vertical lines indicate apices of the drop swing. Binarized images of the image sequence in **a** are shown in **b** with colored borders that correspond to images in **a** and to colored circles in **b**

The axisymmetric computational domain developed to simulate the flow is shown in Fig. 4. A 2-D axisymmetric formulation is adopted to reduce computational cost while preserving accuracy in the quantities of interest. The coaxial jet and core tube are rotationally symmetric by design; the primary geometric departure from axisymmetry is the square cross-section of the sheath duct (12 cm × 12 cm). This is addressed using the hydraulic diameter, $D_h = 4A/P = 0.12$ m, where A is the duct cross-sectional area and P is the wetted perimeter. For a square duct, D_h equals the side length, so the axisymmetric domain is assigned an outer radius of $D_h/2 = 6$ cm, preserving the hydraulic diameter of the square duct. This equivalence is a standard approximation for turbulent duct flows, where corner-driven secondary velocities are weak (typically less than 1–2% of the bulk velocity (Gavrilakis 1992)) and the velocity profile approaches axisymmetry well away from the duct corners, as confirmed by the direct numerical simulation of turbulent square-duct flow (Gavrilakis 1992). Since the pendant drop is located on the tunnel centerline, far from the square walls, the influence of corner geometry on the quantities of interest is negligible.

The core and sheath inlets are modeled using velocity inlet boundary conditions, while the outlet is set as a pressure outlet with a gauge pressure of 0 Pa. All solid walls are treated as no-slip surfaces, and the axis of symmetry is applied along the centerline. Inlet velocities for the core and sheath are specified for each case as summarized in Fig. 4. The domain is discretized using a structured quadrilateral mesh with prism layers near solid boundaries to resolve velocity gradients. The prism layer comprises 15 layers with a first cell height of 0.05 mm, yielding wall y^+ values in the range 0.10–1.62 across all cells, which is consistent with the All-wall-y^+ near-wall treatment model. Local refinement is applied near the jet exit region to accurately capture shear-layer development. We include details of a mesh sensitivity study and a grid convergence index analysis in the Supplement.

Turbulence at the core and sheath inlets is initialized using a turbulence intensity of 1% and a turbulent viscosity ratio of 10, which are common for low free-stream turbulence cases. The sheath flow undergoes successive conditioning before reaching the observation section: it first passes through a HEPA filter, which acts as a high-resistance porous screen analogous to the damping screens shown to suppress turbulent fluctuations by Dryden and Schubauer (Dryden and Schubauer 1947); then through a contraction section; then through a honeycomb laminarizer, which further inhibits lateral velocity components (Loehrke and Nagib 1976); and finally through a second contraction section. Each contraction further attenuates the residual axial turbulence intensity. Longitudinal turbulent fluctuations tend to scale approximately as $1/C$, where C is the contraction ratio, as originally

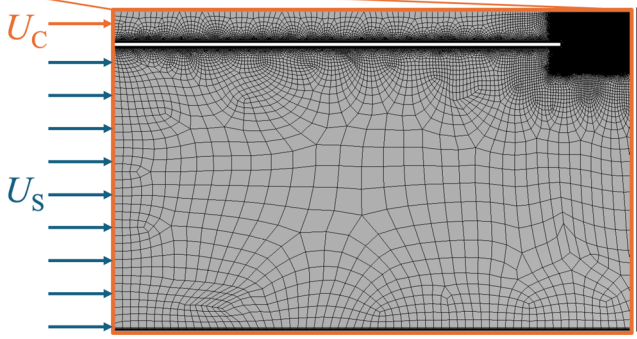

U_S [m/s]	r_U	U_C [m/s]
2.0	0.2	0.4
	0.4	0.8
	0.6	1.2
	0.8	1.6
	1.0	2.0
	1.2	2.4
	1.4	2.8

U_S [m/s]	r_U	U_C [m/s]
4.0	0.2	0.8
	0.4	1.6
	0.6	2.4
	0.8	3.2
	1.0	4.0
	1.2	4.8
	1.4	5.6

Fig. 4 Computational domain, mesh, and boundary conditions used for the CFD simulations

proposed by Prandtl (Prandtl 1933) and later derived theoretically by Batchelor and Proudman (Batchelor and Proudman 1954) via rapid distortion theory. The cumulative effect of this conditioning stack: filter, contraction, honeycomb, and contraction, makes a low inlet turbulence intensity of 1% a physically conservative estimate for the sheath flow at the CFD inlet boundary. Regarding the core inlet turbulence intensity, 1% can be considered a conservative estimate because of the presence of the flush-mounted honeycomb laminarizer discussed in Sect. 2.1. The sensitivity of the velocity profile at the center of the tunnel to the inlet turbulence intensities is included in the online Supplement. We find a maximum velocity difference of 13.3% when the core inlet turbulence varies from 0.5–5%. The jet is not assumed to be fully developed at the exit plane of the core tube. The boundary layer thickness on the tube exterior ranges 1.91–2.91 mm, and the shape factor H ranges from 2.13–2.26. The momentum thickness θ from 0.27–0.39 mm, and $\mathrm{Re}_\theta = 50 - 73$, which signifies that the shear layer stays laminar at the jet exit.

3 Results

3.1 Sheathed coaxial jet-flow produces a turbulent-shearing flow

Using the computational methods described in Sect. 2.2, we calculate the local variation of velocity U and turbulence intensity $I = \sqrt{2k/3}/|U|$, where k is the turbulent kinetic energy, for the experimental volume, shown in Fig. 5. For each r_U at L3, we observe the effects of the boundary layer formed on the inside and outside of the tube wall, as seen in Fig. 5c, f, i, l. Turbulence generated within the boundary layers on the internal and external of the tube wall is the main source of turbulence at L3. Downstream of L3, the boundary layer dissipates and shear is the dominant source of turbulence, as shown in Fig. 5. The value of r_U dictates the magnitude of shear at the core–sheath interface. When $r_U < 1$, the sheath shears the core flow, consequently accelerating the core to a speed similar to the sheath. When $r_U = 1$, no shear occurs between the core and sheath. Thus, the boundary layer alone is responsible for any turbulence and vortical formation downstream. When $r_U > 1$, the core flow shears the sheath flow and thus accelerates the sheath.

The velocity and turbulence at a given height are not isotropic in the transverse direction. Thus, the magnitude of U and I that a pendant drop experiences is influenced by drop size. We plot the streamwise velocity profile and turbulence intensity profile in the transverse direction in Fig. 6 for $r_U = 1.4$, 1.0, and 0.6 at each fixture position. The boundary layer within the core flow gives the velocity profiles a shape characteristic of Poiseuille flow near L3 as seen in Fig. 6a–c. Associated with this boundary layer, there exist high levels of turbulence near the tube wall as shown in Fig. 6d–e. Downstream of L3, we observe the dissipation of the turbulent boundary layer as the slope of the velocity profile decreases as L increases, as shown in Fig. 6a–c. Turbulence generally increases downstream of the tube outlet, as evidenced by the peaks of Fig. 6d–f. Shear at the flow interface gives rise to turbulence above the tube wall, and turbulence spreads radially from the interface as L increases, as shown by Fig. 6d–f.

We take the average of local U and I across individual drop boundaries for each flow condition and fixture position to form the mean velocity U_M and turbulent intensity I_M from our computational model, with the model resolution shown in Fig. 4a. The line across which U_M and I_M are measured is

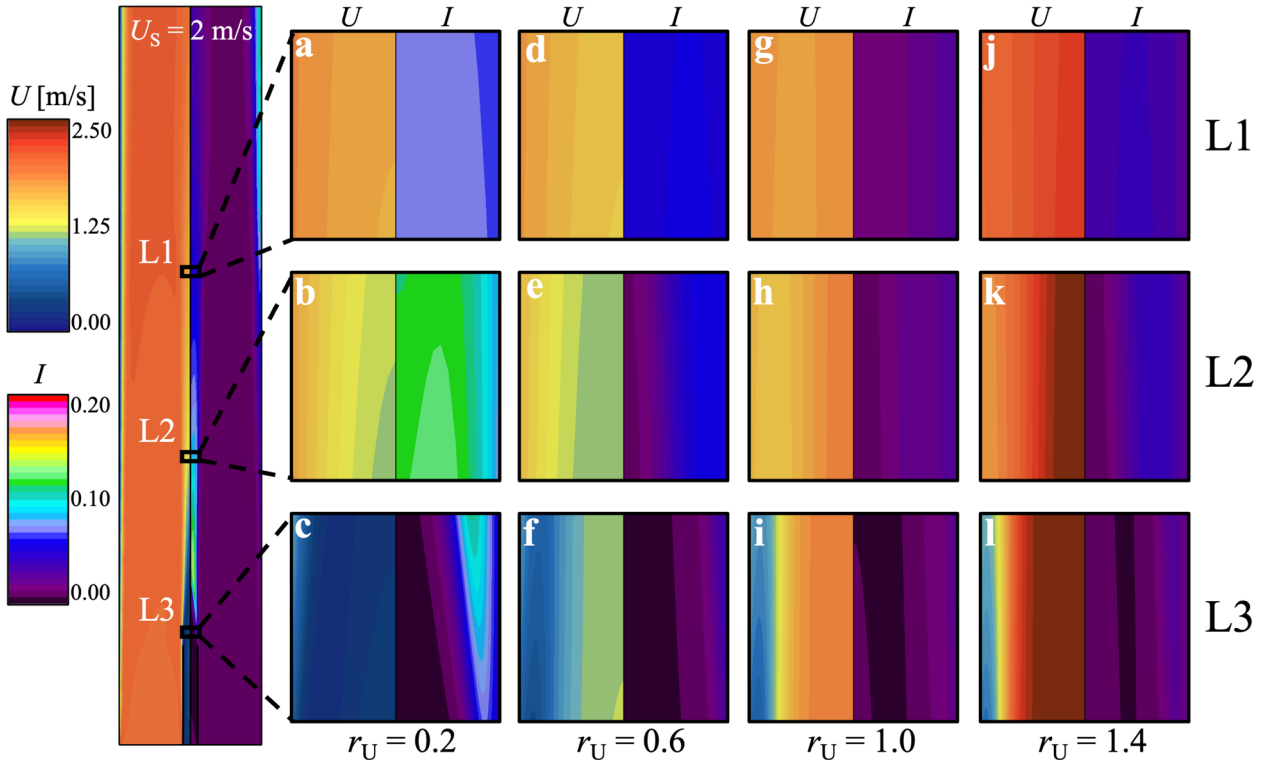

Fig. 5 Plots of CFD predictions of local variation of U and I for U_S = 2 m/s, and r_U = 0.2, 0.6, 1.0, and 1.4 at L1, L2 and L3. We show the large-scale simulation on the left-hand side for U_S = 2 m/s and r_U = 0.2. We plot the local variation of U and I at the three regions, centered about the tube axis at $r = 0$, at which pendant drops are placed for r_U = 0.2, 0.6, 1.0, and 1.4 in **a**–**l**. The bounds of these regions are given by $1.2D_T \times 1.2D_T$

the drop horizontal axis at each fixture position. We plot U_M and I_M for all flow conditions, fixture positions, and drop sizes in Fig. 7. We find that in general, as L increases U increases for $r_U \leq 1$ as seen in Fig. 7a, b. When $r_U > 1$, the flow accelerates between L3 and L2, and experiences little change in U_M between L2 and L1. The acceleration between L3 and L2 is due to a slight expansion of the sheath flow, reducing the effective cross-sectional area of the core flow. When $r_U < 1$ flows are generally more turbulent than when $r_U \geq 1$, as shown in Fig. 7c, d. There exists a minimum in I_M at $r_U = 1.0$, above which I_M increases with r_U. Thus, when shear is minimized, turbulence is also, and increasing shear increases turbulence. The average turbulence across r_U and U_S at each fixture position is 0.04, 0.043, and 0.016 at L1, L2, and L3, respectively. Thus, we find that L2 is the most turbulent location, though only marginally. For $r_U < 0.6$, L2 is far more turbulent than both L1 and L3.

Shear between the core and sheath flow gives rise to a non-uniform velocity gradient that imposes an aerodynamic shear force upon the drop. We define the shear within the flow near the drop as $\tau = \mu(U_S - U_M)/(D/2)$ and the shear force upon the drop as $F_S = \tau(\pi/4)D^2$. We also quantify the aerodynamic drag upon the drop as $F_D = (1/2)\rho C_D \pi (D/2)^2 U^2$. Where C_D is the drag coefficient for a sphere (Morrison 2013) given as

$$C_D = \frac{24}{\mathrm{Re}} + \frac{0.52 \cdot \mathrm{Re}}{1 + (\frac{\mathrm{Re}}{5})^{1.52}} + \frac{0.411(\mathrm{Re} \cdot 2.63 \times 10^{-5})^{-7.94}}{1 + (\mathrm{Re} \cdot 2.63 \times 10^{-5})^{-8}} + \frac{\mathrm{Re} \cdot 0.25 \times 10^{-6}}{1 + \mathrm{Re} \times 10^{-6}}.$$

To compare the relative influence of shear force to drag force upon drop response, we form the shear parameter $\mathcal{S} = F_S/F_D$. We plot $\bar{\mathcal{S}}$ vs r_U in Fig. 8 with colors corresponding to I_M, where $\bar{\mathcal{S}}$ is the average $\mathcal{S}$ across all D for each flow condition. We find that $\mathcal{S}$ is highest for $r_U < 1$ across each fixture position; which also corresponds to an increase in I_M. Beyond $r_U = 1$, $\mathcal{S}$ decreases with increasing r_U across all fixture positions.

3.2 Modal behaviors are simplified in turbulent-shearing flow

We perform $N = 550$ trials of pendant drops consisting of 34 flow conditions for drops $D = 0.981 - 6.9$ mm in diameter, suspended from $D_N = 0.8$-mm and 1.8-mm diameter needles, and placed at three distances from the tube outlet. For fixed inlet conditions (constant U_S and U_C), changing the drop fixture elevation varies the amount of turbulence

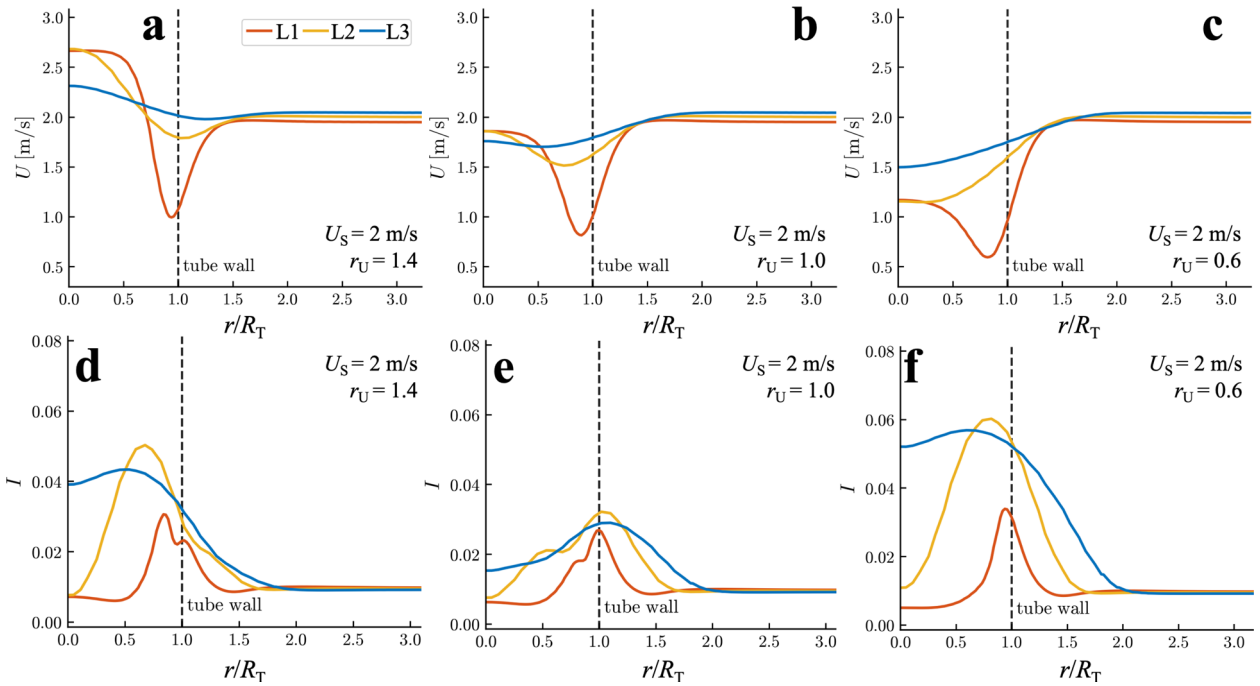

Fig. 6 Plots of the streamwise velocity profile in the transverse direction r/R_T, where $R_T = D_T/2$, are plotted for L1, L2, and L3 for $U_S = 2$ and $r_U = 1.4$, 1.0, and 0.6 in **a**–**c**. The corresponding magnitudes of turbulent intensity for **a**–**c** are plotted against radial position in **d**–**f**. The dashed lines represent the interior tube wall

and drag the drop experiences. We record drop rotational frequency ω and amplitude χ for hanging drops in sheathed, coaxial jet-flow. The dynamics of the drops in this study are best interpreted in the context of pendant drop dynamics in laminar airflow.

In response to laminar airflow, we found that pendant drops exhibit seven behavioral modes characterized by shape deformation and rotation (Dockery et al. 2024). Rotating drops were observed to rotate about an axis of rotation that was either static or dynamic. Drops rotating about a static axis parallel to the needle have little-to-no vertical oscillation as they rotate about the needle, contrasting the vertical oscillation of drops that rotate about a dynamic axis (Dockery et al. 2024). The metric for determining whether a drop has a static or dynamic axis of rotation is given by $y_a P > A$, where y_a, P, and A are the vertical oscillation amplitude, perimeter, and cross-sectional area, respectively. When $y_a P > A$, a dynamic axis of rotation exists (Dockery et al. 2024). Otherwise, the drop rotates about a static axis or does not rotate. Pendant drop shape deformation was determined by tracking the temporal ratio R_M/R_m and measuring its frequency Γ, the shape deformation frequency. R_M and R_m are the maximum and minimum distances from the drop centroid to the drop boundary (Dockery et al. 2024). Since Γ is influenced by drop rotation, we form a dimensionless parameter $\Omega = 2\pi\Gamma/\omega$, the shape deformation factor, useful for describing the magnitude of shape deformation. In our previous work (Dockery et al. 2024), a binary codex was employed to describe the rotation and deformation dynamics of the drops, (α, β). Rotation and rotational axis characteristics are described by α and the magnitude of shape deformation is given by β. For $\alpha = 0$, 1a, and 1b, drops exhibit no rotation, rotation about a static axis, and rotation about a dynamic axis, respectively. For $\beta = 0$, 1a, and 1b, drops exhibit no shape deformation, $1.85 < \Omega < 2.15$, low-frequency shape deformation $\omega < 1.85$ and $2.15 \leq \Omega < 5$, and high-frequency deformation $\Omega \geq 5$, respectively. We employ this same binary codex to describe the behaviors of pendant drops in sheathed, coaxial jet flow.

We display the most common behavioral modes across all needle fixture positions for one needle diameter and all r_U in Fig. 9a. In general, the most common behavioral mode is (1a,0). Second to (1a,0), the most common mode observed for a given r_U is (1b,0). Depictions of these two modes are given in Fig. 9b and image sequences shown in Fig. 9c, d. Unlike drops in laminar flow, we do not observe prominent modes that are characterized by shape deformations. Simply stated, most pendant drops in sheathed coaxial jet flow do not deform as they rotate. We hypothesize that the lack of observed shape deformations in sheathed flow, compared to laminar flow, is due to the presence of turbulence. The interested reader should compare the relative simplicity of mode expression in Fig. 9 in this manuscript to the mode expression in Fig.3 of Dockery et al. (2024) (Dockery et al. 2024).

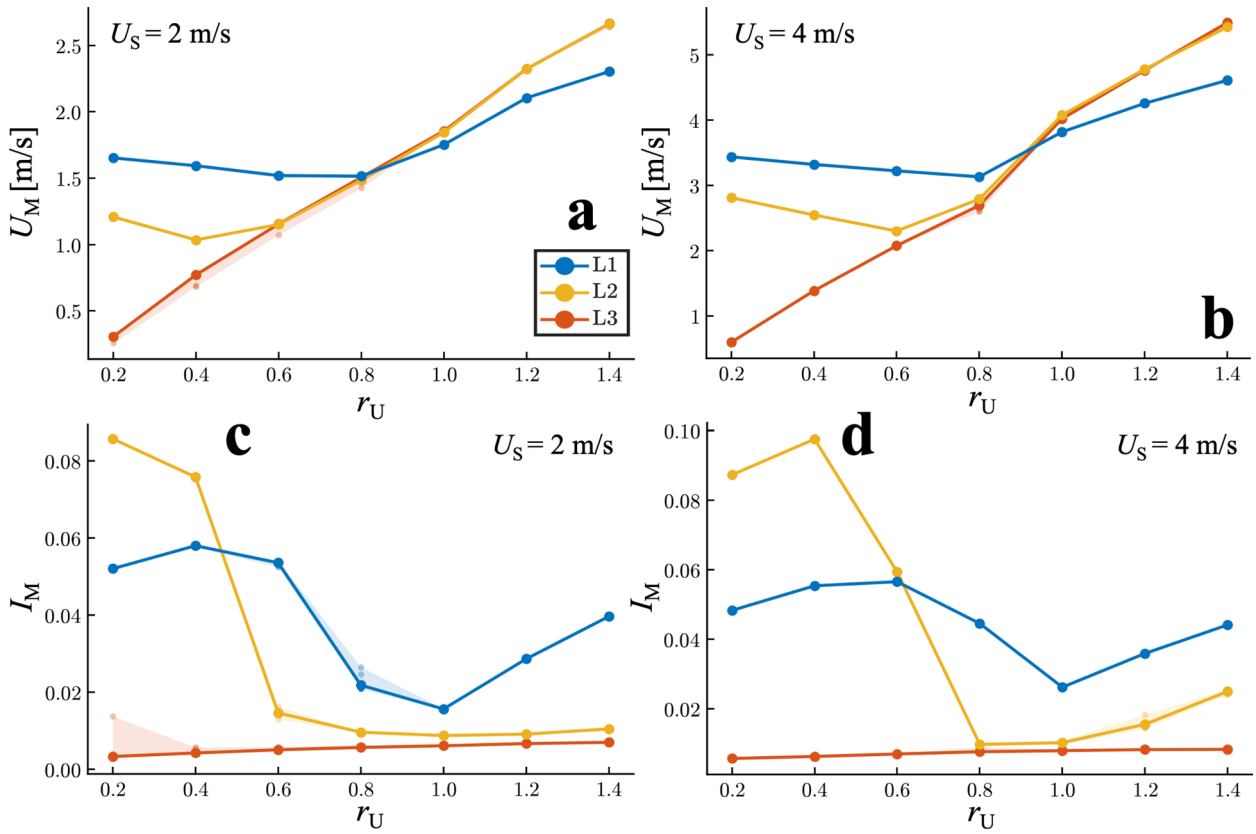

Fig. 7 Variation of CFD prediction of the average velocity magnitude U_M **a**, **b** and turbulence intensity I_M **c**, **d** across all drop diameters D, velocity ratios r_U, sheath flow velocities $U_S = 2, 4$ m/s, and fixture positions L. Individual data points are given by lightly shaded points. The average U_M and I_M across all D at each flow condition is shown by bolded pointed points. The range of U_M and I_M for each condition are given by shaded regions

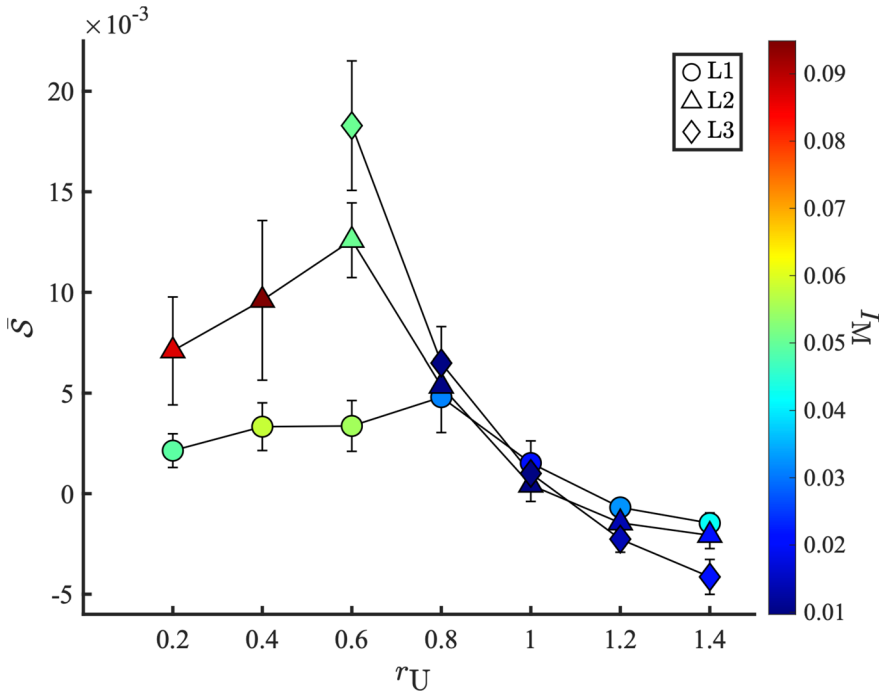

Fig. 8 The average shear parameter $\bar{S}$ is plotted against r_U for each flow condition with error bars. Colors and shapes correspond to I_M and L, respectively

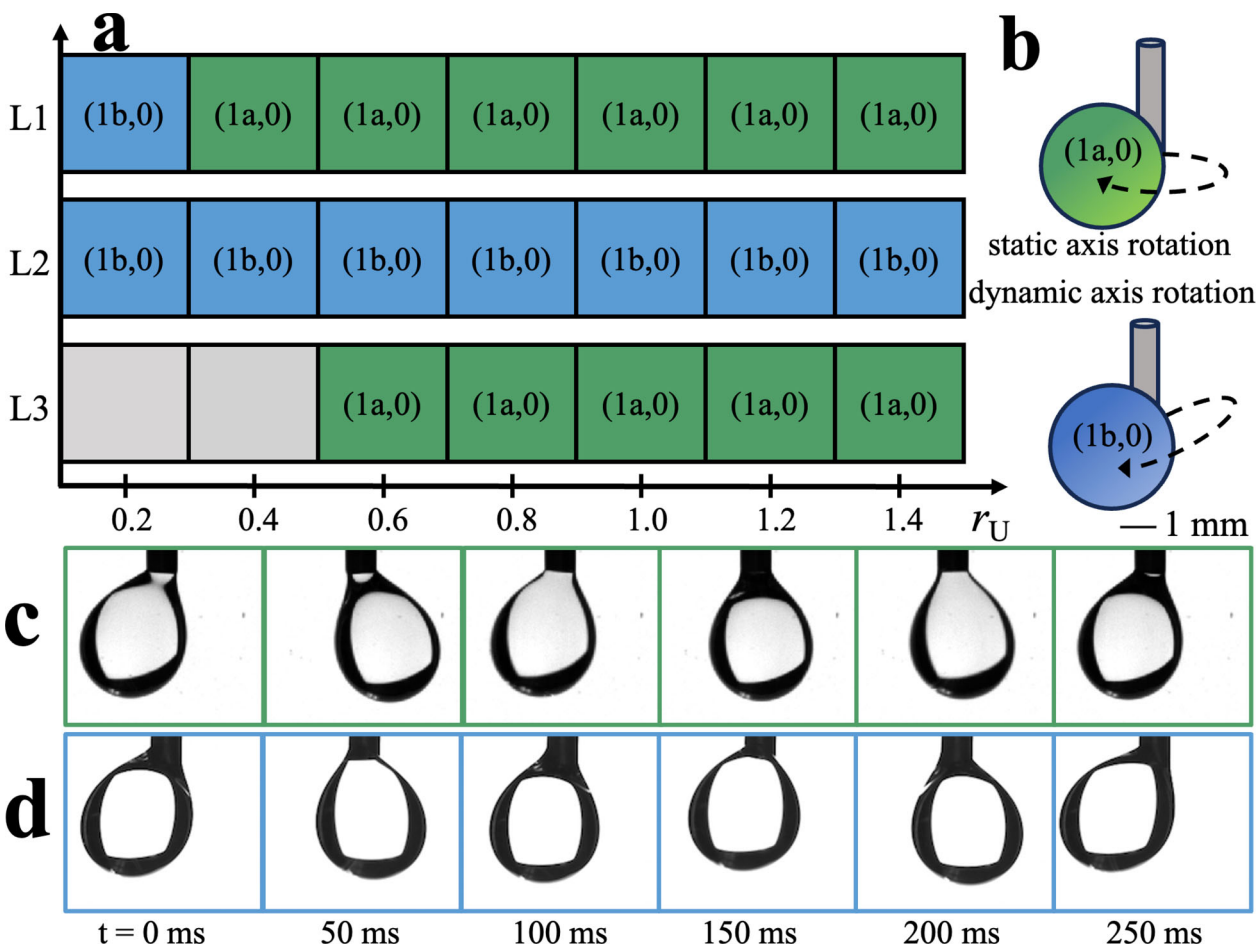

Fig. 9 Pendant drops exposed to ascending, sheathed coaxial jet-flow rotate according to discrete behavioral modes. **a** The most common mode is shown across r_U and levitation height for $D_N = 0.8$ mm. **b** Diagrams of the modes in **a** displaying rotation about static and dynamic axes. Image sequences of drops exhibiting modes (1a,0) and (1b,0) are given in **c** and **d**, respectively

3.3 Pendant drops rotate in turbulent-shearing flows

In the presence of shearing, turbulent flow (sheathed, coaxial jet-flow), pendant drops may oscillate and deform. The rotational behavior of hanging drops in laminar flow is best captured by the use of the Reynolds number. Since measuring the velocity at the drop location would alter the flow field, we employ the model described above (Sect. 2.2) to gather the mean velocity at the drop location U_M, and define $\mathrm{Re} = \rho_a U_M D/\mu_a$ to characterize the behavior of pendant drops in sheathed, coaxial jet-flow. Where ρ_a is air density, D is drop hydraulic diameter, and μ_a is the dynamic viscosity of air.

In our turbulent flow, pendant drops rotate at angular velocities $\omega = 2\pi f$ influenced by drop size, windspeed, needle diameter, and turbulent intensity. We plot ω vs Re for three fixture positions of drops adhered to the same needle of $D_N = 0.08$ cm in Fig. 10a, providing 84 different near-field flows as a result of several combinations of U_S, U_C, and L. This plethora of experimental combinations encompasses a wide range of I_M and U_M for a wide range of drop sizes and allows for a sweeping analysis of pendant drop rotation in our dynamic flow. In general, we find that increasing Re decreases ω, as shown in Fig. 10a, where small drops rotate faster than large drops. While generally small drops rotate faster than large drops in sheathed coaxial jet-flow, the spread of the data across Re for each fixture position in Fig. 10a implies that the law is slightly more complicated compared to laminar flow. We find that the efficacy of the Reynolds number to determine drop rotation depends on the magnitude turbulence that a drop experiences at that location. At L3, where the flow is predominantly laminar, Re does not predict ω. As turbulence increases, Re is a better predictor of drop rotation for a fixed needle size, which is evidenced by the collapse of data for L2 and L1, particularly L2, where turbulence is greatest (Fig. 7c, d). Simply put, the onset of turbulence collapses rotation to be a function of Re only.

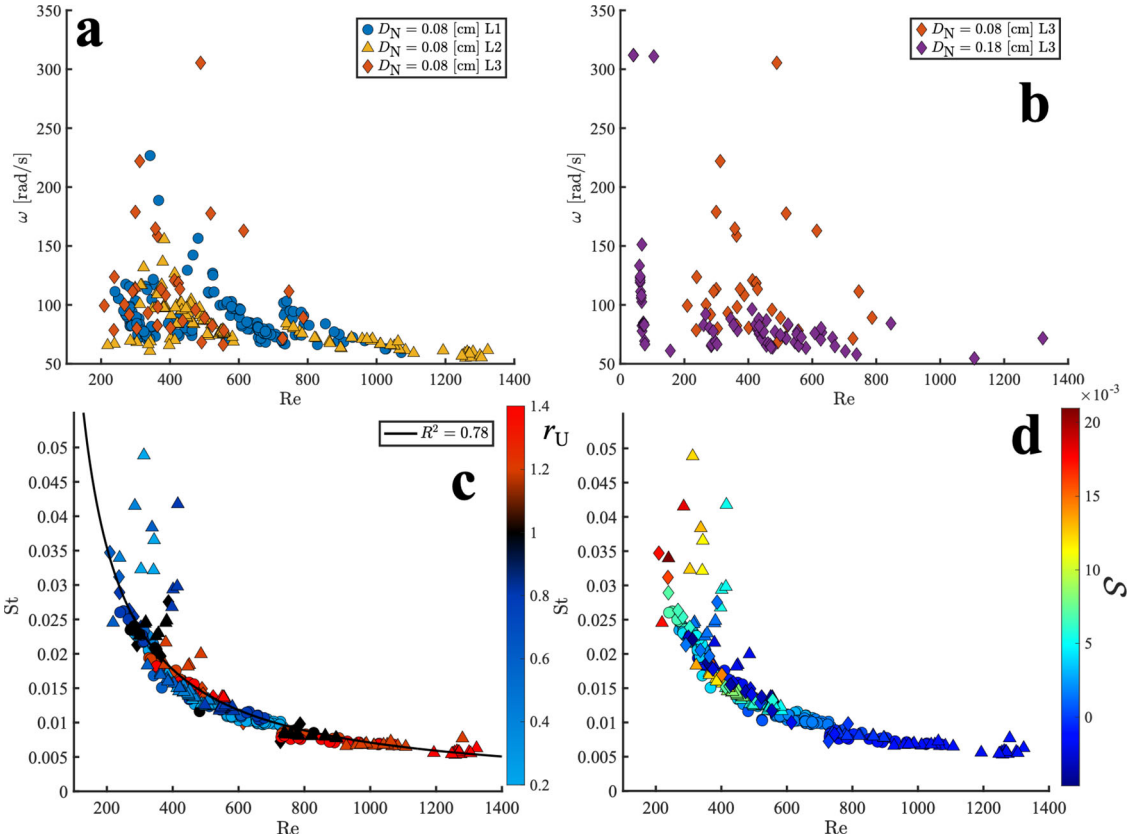

Fig. 10 The rotational dynamics of pendant drops in ascending, sheathed coaxial jet flow are influenced by drop size, core flow velocity, distance from the jet outlet, and the diameter of the needle support. Plot of **a** ω vs Re for one needle at L1, L2, and L3 and **b** for two needles at L3. **c** Re vs St for $D_N = 0.08$ cm and all L, with blue, black, and red points corresponding to $r_U < 1$, $r_U = 1$, and $r_U > 1$, respectively. St $\sim$ Re^{-1} is given as a line of best fit. **d** Re vs St is plotted with colors corresponding to shear parameter $\mathcal{S}$

Given that Reynolds number characterizes wake behavior and dynamics of spheres (Rodríguez et al. n.d.) and tethered-spheres (Williamson and Govardhan 1997; Govardhan and Williamson 1997), it is not surprising that Re captures the dynamics of pendant drops. In our previous study, to elicit the effect of wake structure upon pendant drop dynamics in laminar flow, we adjusted the size of the needle support. Changing the size of the needle either greatly obstructs (large D_N) or slightly obstructs (small D_N) vortical formation in the rear of the drop. We hypothesized that changing the size of the needle support in laminar flows influences ω due to wake interactions with the needle and the needle influence on drop shape (Dockery et al. 2024). We likewise expect needle size to affect drop dynamics in turbulent conditions. We plot ω vs Re for drops adhered to two different needles at L3 in Fig. 10b. At similar Re, drops affixed to smaller needles rotate at a higher ω, a contrast to the dynamics of pendant drops in laminar flows, where drops adhered to larger needles rotate faster than those adhered to smaller needles (Dockery et al. 2024). The decreased rotation for drops affixed to large needles is likely due to a reduction of the coherent vortex shedding behind the drops, influenced by the growing turbulent boundary layer formed at the interface of the core and sheath flow near the tube outlet.

We gain a clearer picture of how rotation varies with airspeed by employing a modified Strouhal number St $= f D/U_M$ that captures the efficacy of a pendant drop to convert the kinetic energy of the ascending airflow to rotation. We plot St vs Re according to fixture position and r_U in Fig. 10c for the data in Fig. 10a. In general, we find that St decreases with increasing Re across r_U and L. This trend indicates that turbulence intensity and shear profile, both of which vary according to L, r_U, and U_S (Sect. 3.1), do not generally augment dimensionless drop rotation. In laminar flows (Dockery et al. 2024), St was also found to decrease with Re. The relationship between Re and St across disparate flows indicates that rotation is generally governed by Re and not so much influenced by the incoming flow profile. It is worth noting that mathematically, St vs Re reduces to f vs U_M^2.

Changes to pendant drop shape alter drop-flow interactions, which affect rotation through changes in drag coefficient, wake formation, and ℓ. In quiescent conditions,

hydrostatic and Laplace pressures compete to form the pendant drop shape. Introducing airflow to the pendant drop, aerodynamic pressure oblately deforms the drop. Changes in D_N/D alter pendant drop shape by changing the length of the three-phase contact line, changing drop curvature, particularly at the neck. Curvature governs the Laplace pressure and thus resistance to deformation. It follows that drops adhered to small needles are more resistant to aerodynamic flattening than drops adhered to large needles, which is consistent with our observations (Dockery et al. 2024). When D_N is held constant, increasing drop diameter weakens the Laplace pressure; subsequently making large drops less resistant to deformation and perturbation. To characterize the influence of modified drop shape upon rotation and to capture drop resistance to perturbation as a function of drop size, needle size, and windspeed, we define pendant drop shape parameter ϵ as a ratio of Laplace pressure($\sim \sigma/D$) to aerodynamic pressure ($\sim \rho_a U^2$), scaled by D_N/D yielding

$$\epsilon \sim \frac{\sigma D_N/D^2}{\rho_a U_M^2}. \tag{1}$$

Equation (1) can be interpreted as a pressure ratio between aerodynamic pressure and a sustaining pressure. We define the sustaining pressure as the capillary force ($\sim \sigma D_N$) acting over the projected drop area to the ascending flow ($\sim D^2$). The aerodynamic pressure deforms drop shape and drives rotation, whereas the sustaining pressure tethers the drop to the needle throughout rotation. Equation (1) can be rearranged as $\epsilon \sim \mathrm{We}^{-1}(D_N/D)$, where $\mathrm{We} = \rho_a U_M^2 D/\sigma$ is the Weber number. Physically, smaller ϵ values correspond to resistance to initial, rotation-inducing perturbations and promotion of oblateness. Accounting for influence of drop shape upon rotation, we define aerodynamic, lateral torque as $\tau_a \sim \rho_a U_M^2 D^2 \ell \epsilon$. Since $\ell \sim D$, our expression for torque reduces to

$$\tau_a \sim \rho_a U_M^2 D^3 \epsilon. \tag{2}$$

The rotation rate of pendant drops can be predicted by examining the energetics of the drop-flow system. The rotational power $P_a \sim \tau_a \omega$ acting upon the drop is damped by the rate viscous dissipation within the drop $\dot{\Phi}$. Viscous dissipation within an oscillating drop (Aalilija et al. 2020) is scales with $\dot{\Phi} \sim \mu_w \int_V \dot{\mathbf{E}} : \dot{\mathbf{E}} dV$, where $\dot{\mathbf{E}}$ is the strain rate tensor, μ_w is the viscosity of water, and V is volume. For a rotating pendant drop $\dot{\mathbf{E}} \sim \omega$, thus $\dot{\Phi} \sim \mu_w D^3 \omega^2$. For steady rotation, $P_a \sim \dot{\Phi}$, or,

$$\rho_a U_M^2 D^3 \epsilon \omega \sim \mu_w D^3 \omega^2. \tag{3}$$

Eq. (3) reduces to $\rho_a U_M^2 \epsilon \sim \mu_w \omega$. Substituting Eq. (1) into Eq. (3) yields $\rho_a U_M^2 D_N \sigma \sim \mu_w \omega \rho_a U_M^2 D^2$. Solving for ω and eliminating like terms give $\omega \sim D_N \sigma/(\mu_w D^2)$. Absorbing constants in our experiments into the scaling prefactor gives $\omega \sim D_N/D^2$. On a single needle (constant D_N),

$$\omega \sim \frac{1}{D^2}, \tag{4}$$

a result consistent with our previous work in laminar flow. The absence of U_M in our scaling law suggests that drop rotation is primarily a function of drop size and less dependent upon U_M.

We recast Eq. (3) to write,

$$\mathrm{St} \sim \mathrm{Re}^{-1}, \tag{5}$$

matching the trend in Fig. 10c. We fit the data of Fig. 10c with Eq. (5), yielding a correlation coefficient $R^2 = 0.78$. Generally, the data fall along the line of best fit, barring some drops at L2 with low r_U. Given that L2 is the region with the highest shear, we plot St vs Re and color the data according to shear parameter $\mathcal{S}$ to elucidate any influence of shear. We find that the rotational data that lies far from Eq. (5) fit has a high $\mathcal{S}$. Some drops at L3 are also characterized by high $\mathcal{S}$, but have lower I_M than the drops rotating at L2. Thus, we posit that deviance from Eq. (5) arises from increased shear and turbulence at L2.

By nature of our flow, drop rotation is subject to influence from boundary conditions. To elicit the influence of D_T upon rotation, we plot St vs D/D_T in Fig. 11a for drops located at the two most turbulent fixture positions, L1 and L2. We find that St decreases with increasing D/D_T along contours of fixed r_U and L, which is a trend that aligns with our dimensionless scaling law $\mathrm{St} \sim \mathrm{Re}^{-1}$. Plotting St vs D/D_T provides convenient boundaries by which to characterize drop behavior. When $D/D_T \lesssim 0.1$, no drop rotation is observed. Generally, when $D/D_T \gtrsim 0.25$, a maximum in drop stability is reached, and drop pinch-off follows. However, there are some points above $D/D_T \approx 0.25$ at L2, that rotate but do not follow the general trend. Simply stated, as drop size approaches that of the tube diameter, rotational behavior is augmented. Given that the deviant points of Fig. 10d are characterized by high $\mathcal{S}$, we re-plot St vs D/D_T and color according to $\mathcal{S}$ in Fig. 11b. We find that these deviant points are likewise characterized by high $\mathcal{S}$, further supporting the idea that when increased shear and turbulence can alter drop behavior from Eq. (5). Since these points lie above the pinch-off boundary, we posit that increased shear delays pinch-off. These deviant points also possess small lateral oscillation amplitudes $x_a/D \lesssim 0.05$.

Thus far, pendant drop response to dynamic, non-uniform disturbances has been reported without direct comparison to uniform disturbances. To observe the influence of turbulence to augment rotation dynamics from those observed in

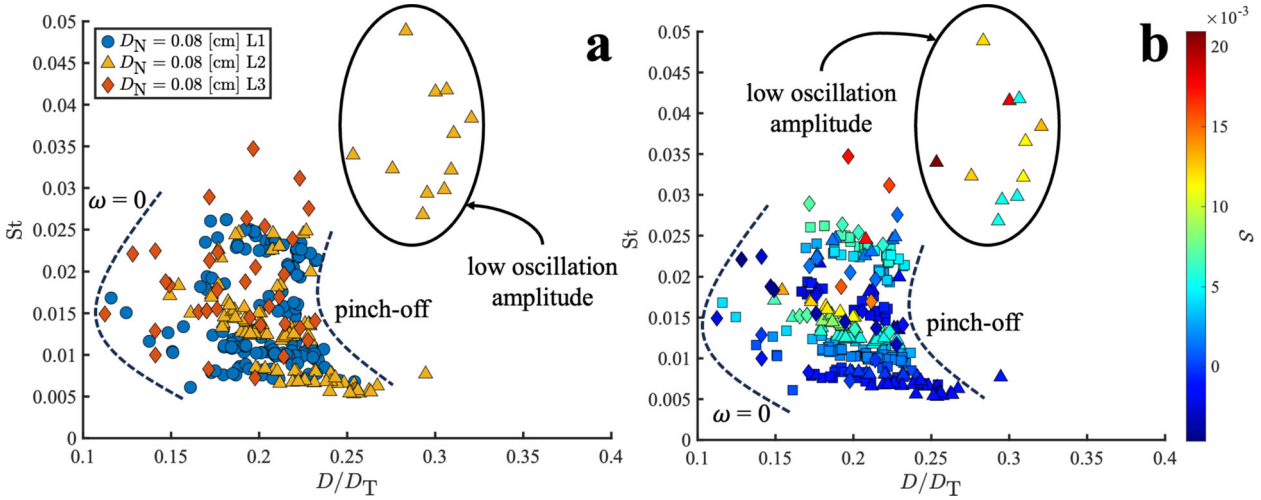

Fig. 11 Plots of St vs D/D_T at flow condition with colors representing fixture position L and shear parameter $\mathcal{S}$ in **a** and **b**, respectively. Dashed lines and circles delineate behavioral boundaries in **a** and **b**

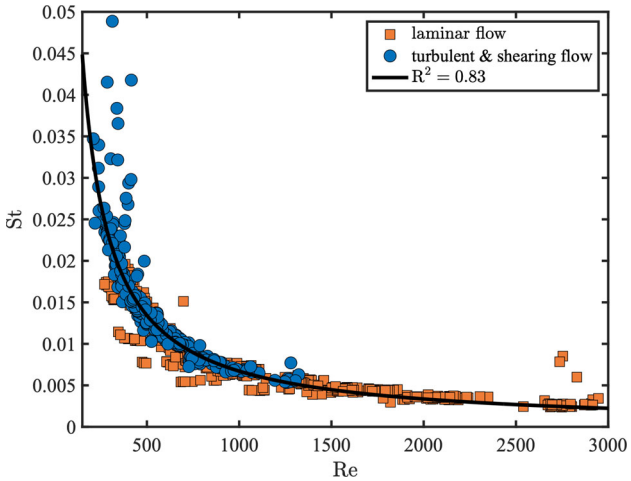

Fig. 12 Dimensionless drop rotation is governed by Reynolds number across laminar and turbulent flows. We plot St vs Re for the data points of Fig. 10d alongside the rotational data of pendant drops in laminar flows. We apply a line of best fit across both data sets following $\mathrm{St} \sim \mathrm{Re}^{-1}$

laminar flows, we plot St vs Re for the colored data points of Fig. 10d and the data of our previous work and apply a line of best fit following $\mathrm{St} \sim \mathrm{Re}^{-1}$ in Fig. 12. We find that across laminar and turbulent flows pendant drop behavior follows $\mathrm{St} \sim \mathrm{Re}^{-1}$ with $\mathrm{R}^2 = 0.83$. The efficacy of the dimensionless scaling law to capture drop rotation across both laminar and turbulent flows, barring regions of increased shear, indicates that dimensionless drop rotation is driven by the Reynolds number.

4 Discussion

4.1 Influences upon drop behavior

The size of pendant drops in this study ranged from $D = 0.98 - 6.9$ mm, a range truncated by pinch-off for our select combinations of r_U and U_S. We posit that if drops with $D < 6.9$ mm were studied, their rotation characteristics would follow Eq. (5). However, drops such that $D/D_T > 0.25$ would not follow Eq. (5) when large enough to be affected by shear at the core–sheath interface for $r_U < 1$. Drops of diameters $D > 6.9$ mm would likely exhibit behavioral modes characterized by shape deformation and off-axis rotation due to a reduction in Laplace pressure, which are observed for large drops in high velocities in laminar flows (Dockery et al. 2024). The deviation from Eq. (5) that occurs as drop size approaches that of the tube diameter is a phenomenon that we would expect to occur for other tube diameters, if tested. Though only one tube diameter is examined in this study, its impact upon rotation is evident by the change in St at large D/D_T. Likely, increasing or decreasing D_T would subsequently scale the value of D/D_T at which rotation deviates from Eq. (5).

In our previous work in laminar flows, we found that the size of the capillary support influences drop rotation; an effect we hypothesized was due to the obfuscation of vortical formation in the drop wake. We likewise investigated the influence of needle diameter to angular velocity in turbulent-shearing flows, but due to the increased number of experimental parameters, we limited our investigation of the role of needle diameter to one fixture position at which we compared two needle diameters. We discovered that near the exit of the core flow, drops on larger needles rotate more slowly than drops on smaller needles, which is the opposite

of what we observed in laminar flows. According to the force balance given in our previous work, the capillary force governs the highest rotational speed a drop can withstand before pinch-off occurs. Likewise, Eqs. (1) and (2) indicate that increasing D_T increases the allowable aerodynamic torque a drop can sustain prior to pinch-off in the lateral direction. Thus, the decrease in ω for increased D_N near L3 is surprising. We assert that this behavior is due to the increased magnitude of shear near the tube outlet. At locations with lower shear, such as L2 and L1 in Fig. 6a–c, we expect that increasing D_N increases ω.

4.2 Sheathed coaxial jet-flow phenomena

The superposition of a co-flowing airstream and a jet creates our sheathed, coaxial jet-flow. While such a flow has not yet been coined as sheathed, coaxial jet-flow; other fluid systems have made use of the phenomena surrounding the superposition of a jet and a co-flowing airstream. Propulsion systems, such as missiles and turbine engines, and car exhausts or fume stacks, both exhaust jets into a co-flowing airstream. Propulsion systems are characterized by $r_U \gg 1$ as the jet-exhaust velocity is significantly higher than any freestream velocity (Mattingly et al. 2016). Automobile engine exhaust of a car in motion operates at varying r_U, where car speed and headwind form U_S. The presence of sheathed coaxial jet-flow across multiple systems merits it characterization in this study and future ones.

Sheathed coaxial jet-flow phenomena are characterized by U_S and r_U. For $r_U < 1$, the velocity field is similar to a jet flow emptying into ambient conditions where the core jet velocity would be $U_C - U_S$. Similarly, for $r_U < 1$, the flow field is similar to that of an airflow passing a long cylinder where the freestream velocity is $U_S - U_C$. Rather than simply studying these similar cases, we employ both the sheath and core flows to mitigate the turbulent instability that a jet emptying into ambient. The range of r_U examined for a fixed U_S in this study was limited to $r_U = 0.2 - 1.4$. We posit that for $r_U < 0.2$, downstream turbulence would continue to increase with decreasing r_U, following the trend of Fig. 7d. For $r_U > 1.4$, local turbulence would likely increase following the trend of Fig. 7d.

The wind tunnel used in this study was first used to observe the oscillation of pendant drops in laminar flows (Dockery et al. 2024). Upon modification, it has now been used to create turbulent-shearing flows and record drop motion within. In addition to studying pendant drops, our wind tunnel can be used to levitate liquid drops, as shown in Fig. 13. Shear at the core–sheath interface for $r_U < 1$ and large U_S creates a downstream region where drop levitation in turbulent-shearing flow is possible for many minutes. At this stable region, the drop levitates above the core airflow and aerodynamic shear prohibits the drop from entering the sheath. We form a pendant drop near L1 above the core and allow the drop to pinch-off, then the drop falls slightly and levitation ensues. Changing the value of r_U allows us to create various levels of turbulence in the flow as well as account for changes in drop size due to evaporation. Employing the pendant drop system used to pinch-off the first levitating drop, we have the ability to inject sequential drops of varying liquids to film their interactions, including coalescence. Such capacities enable the study of liquid mixing in air, quasi-contactless rheology, drops with surface active species, and drops undergoing chemical reactions in which drop oscillation modulates kinetics.

5 Conclusions

We subject pendant drops to vertical, turbulent, and shearing flows and report their dynamics or lack thereof. Turbulence mutes pendant drop dynamics. The turbulent, shearing flow field is provided by a sheathed, coaxial jet in a vertical wind tunnel, a novel flow field that is similar to a coaxial jet. By exhausting a core jet into a suction-type vertical wind tunnel, we subject pendant drops to various magnitudes of nonuniform disturbances arising from turbulence and shear. We employ an Eulerian-based finite-volume CFD solver within Star-CCM+ to provide flow characterizations from which to visualize sheathed, coaxial jet flow and understand pendant drop dynamics therein. The amount of turbulence and shear downstream of the core jet is governed by the velocity ratio, the sheath flow velocity, and the downstream distance from the core jet exit. Pendant drops that rotate in the presence of ascending, turbulent, and shearing flow circumvent the needle support on either a fixed plane (the (1a,0) mode) or experience vertical migration of the centroid (the (1b,0) mode). Generally, rotating drops exhibit mode (1a,0), but in regions of increased shear and turbulence mode (1b,0) is prevalent. Contrary to pendant drop dynamics in laminar flows, modes where drops exhibit periodic shape deformations are not prevalent.

Rotating pendant drops do so at speeds between $50 - 300$ rad/s in turbulent, shearing flows. Drop rotation is influenced by the needle diameter, the velocity ratio between the core and sheath, and the average velocity, turbulence intensity, and shear imposed on the drop. As the drop Reynolds number increases, the drop angular velocity decreases. Similarly, smaller drops rotate faster than larger drops. Drops adhered to small needles rotate faster than those adhered to large needles, the inverse of the observed behavior of pendant drops in laminar flows. Reynolds number becomes a better metric by which to characterize drop angular velocity as the magnitudes of turbulence increase. Turbulence simplifies drop rotation to be primarily a function of Reynolds number. Reynolds number effectively characterizes dimensionless drop rota-

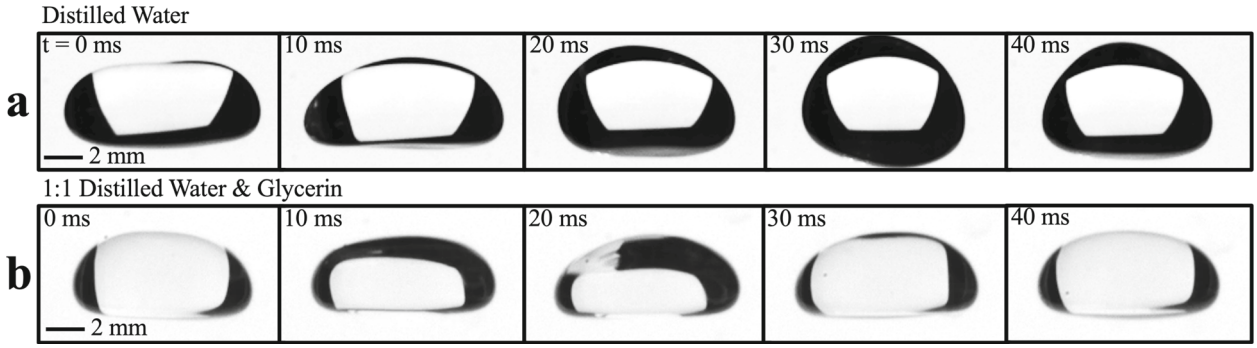

Fig. 13 Drops of distilled water **a** and 1:1 distilled water and glycerin **b** are levitated in turbulent-shearing flow created by sheathed, coaxial jet-flow

tion, given by a modified Strouhal number, and negatively correlates with Strouhal number. By examining the energetics of a rotating pendant drop, the Strouhal number is shown to scale according to an inverse Reynolds number with $R^2 = 0.78$. When dimensionless drop rotation deviates from the scaling law, we find that the drop nears the flow interface above the tube wall and has low oscillation amplitudes. At that interface, increased levels of shear deviate dimensionless rotation from the general trend. Across both laminar and turbulent conditions, the scaling law effectively describes the relationship between drop inertia and dimensionless rotation with $R^2 = 0.83$. Therefore, the onset of turbulence does not greatly augment the dimensionless rotation of pendant drops compared to laminar flows.

Supplementary Information The online version contains supplementary material available at https://doi.org/10.1007/s00348-026-04348-2.

Author Contributions J.D., S.G., and A.D. wrote the manuscript. J.D., M.K., and A.D. edited the manuscript. J.D. performed experiments and curated experimental data. S.G. performed computational fluid dynamics.

Data availability Experimental data collected in this study are openly available in perpetuity at https://doi.org/10.5281/zenodo.20318148.

Declarations

Conflict of interest The authors declare no conflict of interest.

References

Aalilija A, Gandin C-A, Hachem E (2020) On the analytical and numerical simulation of an oscillating drop in zero-gravity. Comput Fluids 197:104362

Angelin I, Naren Shankar R, Sathish Kumar K, Anusindhiya K, Vijayaraja K, Rathakrishnan E (2025) Characterization of lip thickness effects in subsonic coaxial jets with varying velocity ratio. J Appl Fluid Mech 18(10):2518–2534

Au H, Ko NWM (1987) Coaxial jets of different mean velocity ratios, part 2. J Sound Vib 116(3):427–443

Basaran OA, DePaoli DW (1994) Nonlinear oscillations of pendant drops. Phys Fluids 6(9):2923–2943. https://doi.org/10.1063/1.868120

Batchelor GK, Proudman I (1954) The effect of rapid distortion of a fluid in turbulent motion. Quart J Mech Appl Math 7(1):83–103

Bussonnière A, Baudoin M, Brunet P, Bou Matar O (2016) Dynamics of sessile and pendant drops excited by surface acoustic waves: gravity effects and correlation between oscillatory and translational motions. Phys Rev E 93:053106. https://doi.org/10.1103/PhysRevE.93.053106

Clanet C, Lasheras JC (1999) Transition from dripping to jetting. J Fluid Mech 383:307–326. https://doi.org/10.1017/S0022112098004066

Dockery JD, Aydin DY, Dickerson AK (2024) Pendant drop motion and stability in vertical airflow. Phys Fluids 36(2)

Dryden HL, Schubauer GB (1947) The use of damping screens for the reduction of wind-tunnel turbulence. J Aeronautical Sci 14(4):221–228

Emersic C, Connolly PJ (2011) The breakup of levitating water drops observed with a high speed camera. Atmos Chem Phys 11(19):10205–10218. https://doi.org/10.5194/acp-11-10205-2011

Ferrera C, López-Herrera JM, Herrada MA, Montanero JM, Acero AJ (2013) Dynamical behavior of electrified pendant drops. Phys Fluids 25(1):012104. https://doi.org/10.1063/1.4776238

Gavrilakis S (1992) Numerical simulation of low-Reynolds-number turbulent flow through a straight square duct. J Fluid Mech 244:101–129

Govardhan R, Williamson CHK (1997) Vortex-induced motions of a tethered sphere. J Wind Eng Ind Aerodyn 69–71:375–385. https://doi.org/10.1016/S0167-6105(97)00170-0. Proceedings of the 3rd International Colloqium on Bluff Body Aerodynamics and Applications

Haghighi OM, Zargar G, Manshad AK, Ali M, Takassi MA, Ali JA, Keshavarz A (2020) Effect of environment-friendly non-ionic surfactant on interfacial tension reduction and wettability alteration; implications for enhanced oil recovery. Energies 13(15):3988. https://doi.org/10.3390/en13153988

Henderson DM, Pritchard WG, Smolka LB (1997) On the pinch-off of a pendant drop of viscous fluid. Phys Fluids 9:3188

Kandadai MA, Mohan P, Lin G, Butterfield A, Skliar M, Magda JJ (2010) Comparison of surfactants used to prepare aqueous perfluoropentane emulsions for pharmaceutical applications. Langmuir 26(7):4655–4660

Killion JD, Garimella S (2005) Simulation of pendant droplets and falling films in horizontal tube absorbers. J Heat Transfer 126(6):1003–1013. https://doi.org/10.1115/1.1833364

Kwan ASH, Ko NWM (1976) Coherent structures in subsonic coaxial jets. J Sound Vib 48(2):203–219
Latif MT, Brimblecombe P (2004) Surfactants in atmospheric aerosols. Environ Sci Technol 38(24):6501–6506. https://doi.org/10.1021/es049109n
Lee J, Hwang W (2025) Equilibrium shapes and dynamics of pendant drops within a uniform vertical flow. J Fluid Mech 1020:A42
Loehrke RI, Nagib HM (1976) Control of free-stream turbulence by means of honeycombs: a balance between suppression and generation. J Fluids Eng 98(3):342–353
Mattingly JD, Boyer KM, von Ohain H (2016) Elements of propulsion: gas turbines and rockets
Menter FR (1994) Two-equation eddy-viscosity turbulence models for engineering applications. AIAA J 32(8):1598–1605
Moon JH, Kang BH, Kim H-Y (2006) The lowest oscillation mode of a pendant drop. Phys Fluids 18(2)
Morrison FA (2013) An introduction to fluid mechanics. Cambridge University Press, Cambridge. https://doi.org/10.1017/CBO9781139047463
Parkinson LM, Phan CM (2018) Natural vibration of an aqueous pendant drop. Exp Thermal Fluid Sci 90:48–54. https://doi.org/10.1016/j.expthermflusci.2017.09.003
Patankar SV, Spalding DB (1972) A calculation procedure for heat, mass and momentum transfer in three-dimensional parabolic flows. Int J Heat Mass Transf 15(10):1787–1806
Prandtl L (1933) Attaining a steady air stream in wind tunnels. Technical Report TM-726, NACA
Rible GPS, Raza SJ, Traynor CK, Watkins JT, Sebek HP, Bottoms AR, Truscott TT, Dickerson AK (2026) Shape, oscillation modes, and orientation dynamics of aerodynamically levitated nanofluid drops. Phys Rev Fluids 11:053604. https://doi.org/10.1103/s7rj-swb3
Rodríguez I, Lehmkuhl O, Borrell R, Oliva A (2013) Flow dynamics in the turbulent wake of a sphere at sub-critical Reynolds numbers. Comput Fluids 80:233–243. https://doi.org/10.1016/j.compfluid.2012.03.009
Sargison JE, Walker GJ, Rossi R (2004) Design and calibration of a wind tunnel with a two dimensional contraction. https://figshare.utas.edu.au/articles/conference_contribution/Design_and_calibration_of_a_wind_tunnel_with_a_two_dimensional_contraction/23212703
Schmit A, Courbin L, Marquis M, Renard D, Panizza P (2014) A pendant drop method for the production of calibrated double emulsions and emulsion gels. RSC Adv 4(54):28504–28510
Speirs NB, Belden JL, Hellum AM (2023) The capture of airborne particulates by rain. J Fluid Mech 958:A40. https://doi.org/10.1017/jfm.2023.101
Szakall M, Mitra SK, Diehl K, Borrmann S (2010) Shapes and oscillations of falling raindrops—a review. Atmos Res 97(4):416–425
Szakall M, Diehl K, Subir K, Mitra S, Borrmann S (2009) A wind tunnel study on the shape, oscillation, and internal circulation of large raindrops with sizes between 2.5 and 7.5 mm. J Atmos Sci 66(3):755–765
Taraki N, Said Ismail A (2026) Focused liquid pinching in coaxial drop capsule generation. Langmuir 42(8):6344–6353. https://doi.org/10.1021/acs.langmuir.5c06135
Testik FY, Barros AP, Bliven LF (2011) Toward a physical characterization of raindrop collision outcome regimes. J Atmos Sci 68(5):1097–1113. https://doi.org/10.1175/2010JAS3706.1
van Hout R, Murugan S, Mitra A, Cukurel B (2021) Coaxial circular jets–a review. Fluids 6(4):147. https://doi.org/10.3390/fluids6040147
Villermaux E, Rehab H (2000) Mixing in coaxial jets. J Fluid Mech 425(161–185):2000. https://doi.org/10.1017/S002211200000210X
Wijshoff H (2018) Drop dynamics in the inkjet printing process. Curr Opin Colloid Interface Sci 36:20–27
Wilkes ED, Basaran OA (2001) Drop ejection from an oscillating rod. J Colloid Interface Sci 242(1):180–201. https://doi.org/10.1006/jcis.2001.7729
Williamson CHK, Govardhan R (1997) Dynamics and forcing of a tethered sphere in a fluid flow. J Fluids Struct 11(3):293–305. https://doi.org/10.1006/jfls.1996.0078
Willmott GR, Neto C, Hendy SC (2011) Uptake of water droplets by non-wetting capillaries. Soft Matter 7:2357–2363. https://doi.org/10.1039/C0SM00574F
Xie Y, Chen H, An T, Wang Y, Fang H (2025) Pinch-off dynamics of the dripping mode under an axial electric field. Langmuir 41(30):20328–20342. https://doi.org/10.1021/acs.langmuir.5c02712
Yang J, Moradpour N, Au-Yeung L, Tsai PA (2006) Lab-on-a-chip insights: advancing subsurface flow applications in carbon management and hydrogen storage. Lab Chip 26:1352–1393. https://doi.org/10.1039/D5LC00428D
Zhang F, Zhou X (2023) Static and dynamic stability of pendant drops. J Fluid Mech 968:A30
Zheng H, Zhang Y, Li H, Zuhang W, Xie Y, Zhang L (2024) Raindrop deformation in turbulence. Geophys Res Lett 51(9):108627. https://doi.org/10.1029/2024GL108627
Ziqing Pan JP, Trusler M, Jin Z, Zhang K (2025) Interfacial property determination from dynamic pendant-drop characterizations. Nat Protoc 20(2):363–386

Publisher's Note Springer Nature remains neutral with regard to jurisdictional claims in published maps and institutional affiliations.

Springer Nature or its licensor (e.g. a society or other partner) holds exclusive rights to this article under a publishing agreement with the author(s) or other rightsholder(s); author self-archiving of the accepted manuscript version of this article is solely governed by the terms of such publishing agreement and applicable law.